Classical trajectories in polar-asymmetric laser fields: Synchronous THz and XUV emission

Aram Gragossian,[1] Denis V. Seletskiy,[1,2] and Mansoor Sheik-Bahae,[1]
[1] *University of New Mexico, Physics and Astronomy Dept., 1919 Lomas Blvd. NE, Albuquerque, NM 87131, USA*
[2] *Department of Physics and Center for Applied Photonics, University of Konstanz, 78457 Konstanz, Germany*

arXiv:1409.8388v1 [physics.optics] 30 Sep 2014

Synchronous extreme ultraviolet (XUV) and single-cycle terahertz (THz) bursts are generated in argon plasma induced by intense two-color femtosecond laser pulses. Correlations between the intensity of the even and odd high-harmonics and the THz radiation are found by studying the phase-delay between the excitation pulses at 800 and 400 nm as well as the degree of polar asymmetry in the incident electric field. Experiments in both the weak- and strong- polar asymmetric regimes show remarkable agreement with a simple analytical model based on classical electron trajectories in an arbitrary synthetic electric field.

Generation and manipulation of coherent radiation at extreme wavelengths has advanced immensely in the recent years. Significant progress has been made in the field of high harmonic generation (HHG) where the interaction of intense near-infrared laser pulses with rare-gases produces bursts of radiation with spectral content extending into the extreme ultraviolet (XUV) [1, 2] and soft x-ray [3, 4] regions. Along with the advent of novel diagnostic schemes [5–7], this has led to the generation of isolated sub-100 attosecond pulses [8, 9] and can potentially support zeptosecond pulses in the near future [4]. On the other end of the spectrum, advances have been made in the generation and detection of intense coherent sub-harmonic optical waveforms, covering the entire terahertz (THz) frequency spectrum and extending into the mid- and near-infrared [10–13]. Electromagnetic pulses in both spectral extremes can be efficiently generated and manipulated using a two-color excitation scheme where the fundamental driving pulse is combined with its second harmonic (SH) in a rare gas plasma [9, 14–19].

The generation of high harmonics in rare gases follows a non-perturbative mechanism, with its salient features captured by a classical three-step model [20, 21]. In this picture, electrons are liberated in a tunnel ionization process and accelerated every half cycle of the driving laser pulse. Depending on their birth time, a fraction of these electrons can acquire sufficient kinetic energy to trigger high-energy photon emission upon recombination with the parent ion. This simple, insightful model was confirmed by a quantum-mechanical approach in the strong-field-approximation [22] followed by a detailed conversion efficiency analysis [23, 24]. A rigorous description of the ionization and the ensuing electronic wavepacket dynamics was performed by numerical evaluation of time-dependent Schrödinger equation (TDSE) [25–27]. The polar symmetry of the laser field and the centro-symmetry of the gaseous media cause the generated bursts of XUV emission to contain only odd harmonics of the carrier frequency ω_0. This symmetry can be broken by injecting a small fraction of phase-locked SH field at $2\omega_0$, resulting in emission of odd as well as even harmonics [14, 15, 17, 28–30]. The resulting polar asymmetry can be coherently controlled by the relative phase difference between these fields. Using this scheme, it was shown that the birth of attosecond pulses can be controlled with high precision [28, 31, 32]. Two-color excitation has also been employed to generate controlled bright single-cycle THz radiation in gaseous targets [18]. While initial observations were qualitatively consistent with a $\chi^{(3)}$ model [18, 33, 34], a satisfactory quantitative description was given by a classical macroscopic plasma current model that essentially uses the first two steps of the 3-step model without recombination [19, 35]. In this picture, some of the electrons that do not return to the parent ion may create a transient net current (following the pulse envelope) with a bandwidth extending to tens of THz [19]. The asymmetric (drift) trajectories of the ionized electrons adequately describe the key features of the THz experiments. The TDSE has also been used to analyze certain experimental features in the THz radiation [14, 36, 37]. The intriguing similarities in the physics of XUV and THz generation together with the practical implications of temporal synchronization provide motivation for probing their correlations and coherent control. In this letter, we investigate simultaneous generation of XUV and THz radiation under conditions of weak and strong polar asymmetry in co-polarized two-color excitation. We present a simple and intuitive analytical expression based on classical electron trajectories and tunnel ionization (extended 3-step model) that well describes the main experimental features of HHG in both polar asymmetry regimes. This model successfully explains the observed correlations of XUV emission with the synchronously-generated THz radiation.

The experimental setup for synchronous generation and detection of XUV and THz radiation is shown schematically in Fig. 1. A train of 1 kHz, 40 fs pulses with a center wavelength of 800 nm produces high har-

monics when focused onto the output of an argon gas injection nozzle with peak intensity of $5 \times 10^{14}\ W/cm^2$. Good spatial and temporal coherence properties of the high harmonics are ensured by placing the nozzle after the focus [38].

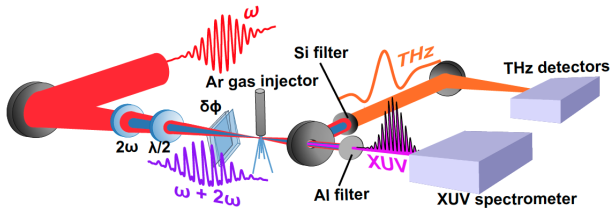

FIG. 1. Schematic of the experimental setup.

The SH of ω_0 is generated in a 150 μm type-I BBO crystal, the orientation and position of which control the conversion efficiency of SH in the range of 0.5% to approximately 10%. Parallel polarizations of the two fields are ensured by an ultra-thin, true zero-order half-wave plate for the fundamental wavelength. As expected from symmetry arguments and confirmed by measurements, this results in linearly polarized THz and XUV emission. A pair of glass wedges controls the relative phase $\delta\phi$ and hence the degree of asymmetry between two pulses with an accuracy $\approx \pi/5$ that is independently calibrated in a separate experiment [39]. All of these optical components are placed in a low background pressure chamber to ensure minimal phase-slip between the fundamental and SH pulses. An off-axis parabolic mirror is located after the gas nozzle and serves to collimate the THz field out of the vacuum chamber through a silicon viewport. This window also acts as an optical filter to remove the excitation light. A 500 μm diameter central hole of the parabolic mirror transmits the low-divergence XUV beam. It then passes through a 200 nm thick aluminum filter and is routed to a grazing-incidence XUV spectrometer (McPherson Inc.) as shown in Fig. 1. Terahertz emission is field-resolved with electro-optic sampling and direct detected by a pyroelectric detector. Polarization states of the XUV and THz pulses are ensured using polarization-dependent anisotropy of the grating reflectivity and a broadband polarizer, respectively, both with contrast better than 10 to 1.

Simultaneous emission of XUV and THz radiation is measured as a function of phase delay $\delta\phi$ within the synthetic excitation pulse. We consider two regimes of weak and strong polar asymmetry corresponding to low ($\leq 1\%$) and high ($\geq 10\%$) SH injection, respectively, as referenced to the average power of the fundamental pulse train. Under the condition of strong SH injection, the measured HHG spectrum contains even and odd harmonics with both exhibiting maxima corresponding to $\delta\phi \approx m\pi$ for all of the harmonic orders (Fig. 2). Phase delay also leads to modulation of the THz power, but with the maxima around $\delta\phi \approx (2m+1)\pi/2$, corresponding to fully polar symmetric two-color excitation. The anti-correlated nature of the emissions can be qualitatively understood by considering classical electron trajectories. According to the 3-step model, those electrons responsible for HHG follow closed trajectories that terminate in a collision with a parent ion within a half-cycle of the driving pulse. This cannot result in any net charge displacement (or current) at low frequencies.

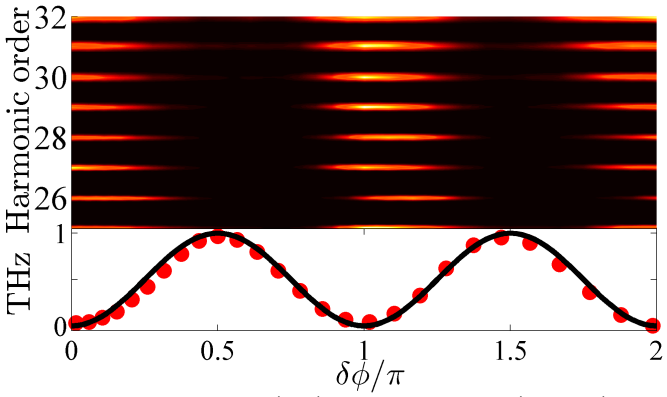

FIG. 2. High harmonics (top) and THz energy (bottom) as a function of the relative phase $\delta\phi$. Dots are measurements and the black line is calculated THz using plasma current model.

THz generation, on the other hand, is described by a classical macroscopic plasma current model where tunnel ionization is followed by electron acceleration. This builds with each consecutive half-cycle of the 2-color pulse to generate a net low-frequency current [19, 35]. Such accumulation is only possible if the instantaneous drift velocity (v) profile has polar asymmetry. Because $v(t) \propto \int E dt'$, this corresponds to the case of polar-symmetric excitation field E with $\delta\phi = (2m+1)\pi/2$ [19]. The THz emission is shown to follow $\sin^2(\delta\phi)$, in close agreement with our observation (Fig. 2). It is instructive to develop an analytical model and test its sensitivity to other experimental parameters. Corkum's Simple Man's Model [20] is broadened to obtain a compact but qualitative expression for the HHG spectrum under arbitrary linearly polarized synthetic excitation. Our "extended three-step "(ETS) model captures the observed details for both weak and strong asymmetry.

We emphasize that the following "intuitive"treatment of HHG is based on classical trajectories. By its very nature, it cannot be rigorous as it makes a quantum leap (literally) by assuming that each re-collision produces a photon in a deterministic way. Our primary objective is to elucidate the critical role of the polar asymmetry of the excitation field, i.e. understanding the effect of SH power (η) and its relative phase delay ($\delta\phi$) with with respect to the fundamental. We are not concerned with the absolute magnitudes, conversion efficiency, or propagation evolution including the phase-matching requirements. We begin with two-color laser pulses having a combined local (fixed position along the propagation axis) electric field

$E(t) = E_1(t) + E_2(t)$ with $E_1(t) = A_0(t)cos(\omega_0 t)$ and $E_2(t) = \sqrt{\eta}A_0(t)cos(2\omega_0 t + \delta\phi)$, where A_0 is the pulse envelope. After an ionizing event, the transverse electron trajectories $x(t_i, t_r, \delta\phi)$ are obtained from solution of the classical equation of motion ($m_0\ddot{x} = -eE$) given a birth time t_i and no initial momentum. As in the one-color excitation, the return times (t_r) for each trajectory are the solution of $x(t_i, t_r, \delta\phi) = 0$, with a return kinetic energy $U(t_i, t_r, \delta\phi) = m_0\dot{x}(t_i, t_r, \delta\phi)^2/2 = U_p F(t_i, t_r, \delta\phi)$, where $U_p = e^2A_0^2/4m_0\omega_0^2$ is the pondermotive energy. Exploiting the well-known relationship between the field amplitude and the photon number, we take the spectral amplitude of the emitted harmonics to vary as $|E_H(\omega)| \propto \sqrt{\hbar\omega\dot{\rho}}$ where $\dot{\rho}(t_i)$ is the ionization rate at a given birth time t_i for electron trajectories having return energy U that satisfies $U(t_i, t_r, \delta\phi) + I_p = \hbar\omega$ with I_p denoting the ionization potential of the gas. Next, we assign a relative spectral phase ωt_r to such a trajectory; this signifies the distinct re-collision (arrival) times of each trajectory "bunch"in the time domain. The total local HHG electric field $E_H(\omega, \delta\phi_r)$ is then obtained by summing the contributions from all trajectories during the excitation pulse (up to four per optical cycle of the fundamental) having the same return energy ($\hbar\omega$):

$$E_H(\omega, \delta\phi) \propto \sum_{t_i} sgn\left(E\left(t_i, \delta\phi\right)\right)\sqrt{\omega\dot{\rho}\left(t_i, \delta\phi\right)}e^{i\omega t_r(t_i, \delta\phi)}, \quad (1)$$

where the sum is over all the $t_i(\omega, \delta\phi)$'s that satisfy $U(t_i, t_r, \delta\phi) + I_p = \hbar\omega$. The sign function $sgn(E)$ is introduced to ensure the centro-symmetry of the medium, implying that the radiation from right and left trajectories have opposite polarity. The ionization density is calculated from $\dot{\rho}(t) = [\rho_0 - \rho(t)]w(|E(t)|)$ where $w(.)$ is the tunneling ionization rate [40, 41]and ρ_0 is the initial gas density. For simplicity, Eq. 1 is derived assuming uniform spectral density of the trajectories, i.e. $|dU/dt_i|$ =constant, which is a fair approximation for the plateau harmonics. Calculated transit times ($\Delta\varphi = \omega_0(t_r - t_i) = \varphi_r - \varphi_i$), return energy U, and electric field E are plotted in Fig. 3 versus $\varphi_i = \omega_0 t_i$. Similar to the case of one-color excitation, the long and short trajectories are identified as those corresponding to before and after the peak of returned energies in each half-cycle, respectively.

Fig. 4 shows the calculated HHG spectra $S(\omega, \delta\phi) = |E_H|^2$ (middle column) using Eq. 1 in excellent qualitative agreement with our measurements (left column) for both weak ($\eta = 0.005$) and strong ($\eta = 0.1$) polar asymmetry. For typical experimental conditions in the 2-color excitation scheme, most observations correspond to the mid-harmonics within the plateau ($1.5I_p < \hbar\omega < 1.5U_p$). Given the peak intensities involved in these experiments ($\approx 5\times10^{14}\ W/cm^2$), this corresponds to $\approx$ H16-H26 harmonics of the fundamental at 800 nm. In this regime, the emission is dominated by the long electron trajectories as evident from the larger amplitude of $\dot{\rho}$ at the birth time of these trajectories. The contribution of short trajectories becomes noticeable only at energies approaching the cut-off (not shown).

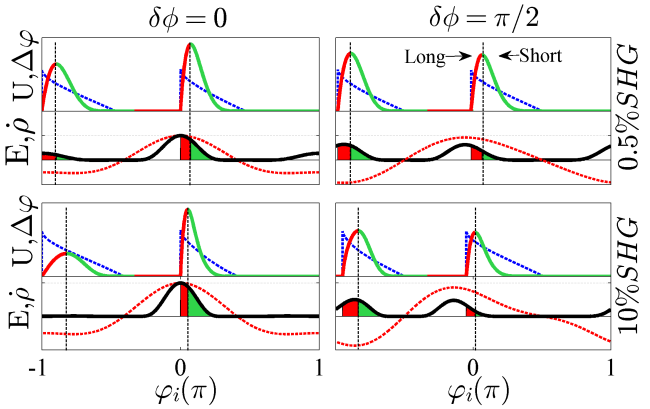

FIG. 3. The electron transit time (phase= $\Delta\varphi/\pi$,blue) and return kinetic energy U, the electric field E (doted red) and $\dot{\rho}$ (black) versus the ionization time (phase) for two extreme relative phase delays assuming 0.5% and 10% SHG for top and bottom rows, respectively. Colored areas represent contributions from long (red) and short (green) trajectories separated by vertical dashed lines.

The simplicity of our model allows us to identify the underlying physical mechanisms manifested in the experimental results. In the high polar asymmetry case (Fig. 3 bottom), the extreme nonlinearity in the tunnel ionization rate suppresses the amplitude ($\dot{\rho}$) in the adjacent half cycle (for $\delta\phi = m\pi$), thus leading to a full-cycle periodicity of the HHG signal in the time domain. Fourier analysis shows how this leads to the formation of both odd and even harmonics. At phase delays corresponding to $\delta\phi = (2m+1)\pi/2$, the time-domain signal returns to half-cycle periodicity but with much lower amplitude (Fig. 3). The production of XUV is thus peaked at $\delta\phi \approx m\pi$, which is also anti-correlated in $\delta\phi$ dependence with the THz emission process (Fig. 2).

More striking is the agreement of this simple model with the results of weak polar asymmetry (SHG=0.5%, Fig. 4), where two main features of our experimental data and others [28, 29, 32, 42]) are reproduced. We note that even harmonics appear out-of-phase with the odd harmonics. Another curious feature is the small shift in the HHG maxima or minima with phase delay $\delta\phi$, as depicted in Fig. 4 with a line of slope $\approx \pi/50$ or 27 attoseconds per harmonic. Dudovich *et al.* [28] exploited this shift to deduce the phase of the electron wavepacket and to control the creation of attosecond pulses. In the case of weak polar asymmetry, the effect of the ionization rate is not as dominant and the observed HHG spectral behavior is determined instead by the spectral interference of emitted radiation from the first and the second

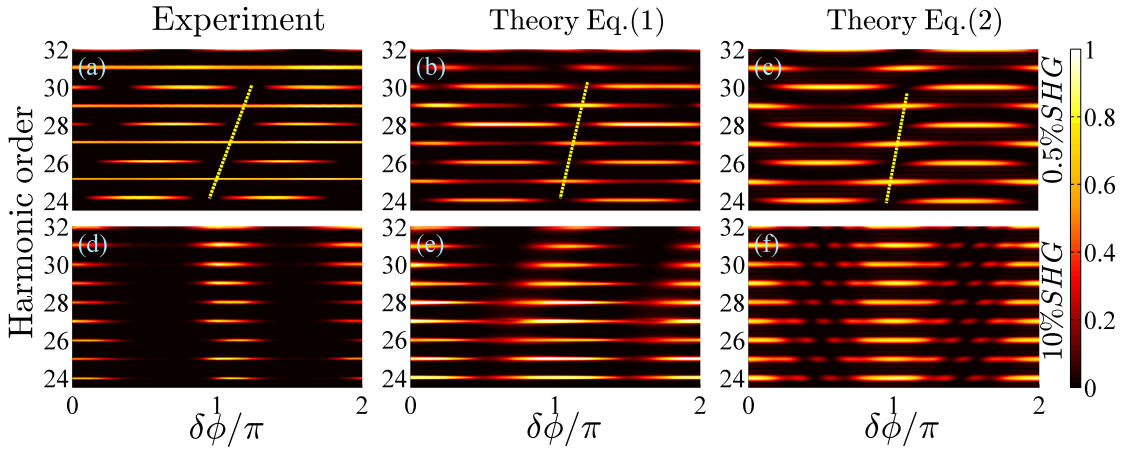

FIG. 4. Comparison of experimental (a and d) and theoretical [Eq. 1 (b and e), Eq. 2 (c and f)] spectra of XUV emission excited by pulses with weak (0.5% SHG, top) and strong (10% SHG, bottom) polar asymmetry.

half cycles in each optical period of the fundamental field. The injection of the small SH signal breaks the half-cycle periodicity resulting in the generation of even harmonics in addition to odd harmonics. The variation of the spectral phase, $\varphi_q = \omega t_r$, with harmonic order ($q = \omega/\omega_0$) and the phase delay $\delta\phi$ explains the shift in the harmonic peaks shown in Fig. 4. The interference between two adjacent long (and short) trajectories involves the differential spectral phase $\Delta\varphi_q = (\varphi_r^{(1)} - \varphi_r^{(2)})q$ with (1) and (2) indicating the first and second half-cycles. For a given ω, this quantity can be evaluated numerically using the classical equations of motion presented earlier. With no SH injection ($\eta = 0$), we have $\Delta\varphi_q = q\pi$ for both short and long trajectories due to half-cycle periodicity. Deviation of $\Delta\varphi_q$ from π due to SH injection and its dependence on the phase delay can be evaluated numerically to the first order. For mid- harmonics, this variation is fit with the $\Delta\varphi_q^{(L)}(\omega, \delta\phi) \approx q(\pi + 1.33\sqrt{\eta} \times \sin(\delta\phi - 0.060q))$ and $\Delta\varphi_q^{(S)}(\omega, \delta\phi) \approx q(\pi + 1.8\sqrt{\eta} \times \cos(\delta\phi + 0.075q))$ for long and short trajectories, respectively. We note that the empirical slope of 0.06 radians ($\approx \pi/50$) per harmonic for $\Delta\varphi_q^{(L)}$is in close agreement with our measurements and more generally with all the reported experimental mid-harmonic data. The broad applicability of this finding highlights the validity of a classical description of the electron trajectories.

To further emphasize this point, we simplify the expression in Eq. 1 by assuming that $\dot{\rho}$ scales as $|E|^Q$ and take the SH injection as a perturbation. A comparison with the static tunnel ionization rate indicates that $Q \approx$ 7-9 for the laser intensities in these experiments. Considering the dominant birth times to be near the peaks of each cycle, two adjacent long trajectories will take relative amplitudes $A^{\pm} \approx (1 \pm \sqrt{\eta}\cos(\delta\phi))^{\frac{Q}{2}} \approx \exp(\pm\frac{Q}{2}\sqrt{\eta}\cos(\delta\phi))$. From Eq. 1, a square pulse having N cycles will then produce an HHG spectrum:

$$S(\omega, \delta\phi) \propto \left|\sinh\left(\frac{Q}{2}\sqrt{\eta}\cos(\delta\phi) - i\frac{\Delta\varphi_q^{(L)}}{2}\right)\right|^2 C_N(q), \quad (2)$$

where $C_N(q) = \sin^2(N\pi q)/\sin^2(\pi q)$ is a comb function. A plot of this simple expression assuming Q=8 for 0.5% and 10% SH injection is shown in right column of Fig. 4, where the main features of the observations are reproduced. We have assumed N=4 cycles for clarity. At higher harmonics approaching the cut-off, the amplitude of the short trajectories becomes comparable to the long trajectories leading to additional interference and consequently more complex dependence of the HHG spectra on the phase delay. As indicated by the empirical fits to the differential phases $\Delta\varphi_q^{(L)}$ and $\Delta\varphi_q^{(S)}$ given above, the modulation of the HHG spectra by the phase delay for the long and short trajectories has opposite signs (-0.060 vs +0.075), which causes this modulation to reverse at higher harmonics. This behavior is in qualitative agreement with experiments that were explained by the semi-classical calculations [32, 42]. A more detailed analysis of this regime is beyond the scope of this letter, and will be addressed in later publications.

The excellent agreement between experiments and the ETS model points to the robustness of the original 3-step model in its semi-classical approximation of high-harmonic generation. For the case of strong injection, the ETS model in combination with the plasma current model verifies the observed anti-correlated dependence of XUV and THz on the relative phase parameter $\delta\phi$. In the regime of weak injection, this dependence is more complicated due to an additional phase shift depending on the harmonic order. In this regime, the Coulomb potential has been argued to be responsible for deviations in the correlation of XUV and THz emission from the predictions of the plasma current model [42]. Our results clarify the critical role of classical long electron trajectories and their differential re-collision times from each adjacent

half-cycle in modulating the XUV spectrum under conditions of both weak and strong injection. Additionally, the ETS model naturally includes a unified description of XUV and THz emission within the framework of classical trajectories, experimentally verified for conditions of strong injection.

In conclusion, we investigated simultaneous emission of THz and XUV radiation from two-color laser-driven plasmas. By controlling the polar asymmetry of the synthetic driving field, we observe and quantify correlations between emission of ultrashort bursts of coherent THz and XUV emission. We presented an extended 3-step model based on the classical electron trajectories that provides exceptional agreement with experimentally observed XUV spectra in the regimes of weak and strong second harmonic injection. Furthermore, the agreement of the observed correlation features in the THz and XUV emission with our theory suggests that the two processes have the same physical origin, only with different electron trajectories.

The work at UNM was partially supported by the NSF under Award DMR-1207489, and by the Los Alamos National Laboratory (LDRD) program 20120246ER. DVS acknowledges support by the NSF (Grant No. 1160764) and partial support by the EU FP7 Marie Curie Zukunftskolleg Incoming Fellowship Program, University of Konstanz (Grant No. 291784).

[1] A. McPherson, G. Gibson, H. Jara, U. Johann, T. S. Luk, I. A. McIntyre, K. Boyer, and C. K. Rhodes, J. Opt. Soc. Am. B **4**, 595 (1987).
[2] P. Antoine, A. L'Huillier, and M. Lewenstein, Phys. Rev. Lett. **77**, 1234 (1996).
[3] M. Drescher, M. Hentschel, R. Kienberger, G. Tempea, C. Spielmann, G. A. Reider, P. B. Corkum, and F. Krausz, Science **291**, 1923 (2001).
[4] T. Popmintchev, M.-C. Chen, D. Popmintchev, P. Arpin, S. Brown, S. Aliauskas, G. Andriukaitis, T. Baliunas, O. D. Mcke, A. Pugzlys, A. Baltuka, B. Shim, S. E. Schrauth, A. Gaeta, C. Hernndez-Garca, L. Plaja, A. Becker, A. Jaron-Becker, M. M. Murnane, and H. C. Kapteyn, Science **336**, 1287 (2012).
[5] F. Krausz and M. Ivanov, Rev. Mod. Phys. **81**, 163 (2009).
[6] M. Chini, K. Zhao, and C. Chang, Nature Photon. **8**, 178 (2014).
[7] K. T. Kim, D. M. Villeneuve, and P. B. Corkum, Nature Photon. **8**, 187 (2014).
[8] E. Goulielmakis, M. Schultze, M. Hofstetter, V. S. Yakovlev, J. Gagnon, M. Uiberacker, A. L. Aquila, E. M. Gullikson, D. T. Attwood, R. Kienberger, F. Krausz, and U. Kleineberg, Science **320**, 1614 (2008).
[9] K. Zhao, Q. Zhang, M. Chini, Y. Wu, X. Wang, and Z. Chang, Opt. Lett. **37**, 3891 (2012).
[10] Q. Wu and X. Zhang, Appl. Phys. Lett. **68**, 1604 (1996).
[11] J. Dai, X. Xie, and X.-C. Zhang, Phys. Rev. Lett. **97**, 8 (2006).
[12] A. Sell, A. Leitenstorfer, and R. Huber, Opt. Lett. **33**, 2767 (2008).
[13] E. Matsubara, M. Nagai, and M. Ashida, Appl. Phys. Lett. **101** (2012).
[14] I. Kim, C. Kim, H. Kim, G. Lee, Y. Lee, J. Park, D. Cho, and C. Nam, Phys. Rev. Lett. **94**, 2 (2005).
[15] J. Mauritsson, P. Johnsson, E. Gustafsson, A. L'Huillier, K. J. Schafer, and M. B. Gaarde, Phys. Rev. Lett. **97**, 013001 (2006).
[16] H. Roskos, M. Thomson, M. Kre, and T. Lffler, Laser Photon. Rev. **1**, 349 (2012).
[17] L. Brugnera, D. J. Hoffmann, T. Siegel, F. Frank, A. Zair, J. W. G. Tisch, and J. P. Marangos, Phys. Rev. Lett. **107**, 153902 (2011).
[18] D. J. Cook and R. M. Hochstrasser, Opt. Lett. **25**, 1210 (2000).
[19] K. Y. Kim, J. H. Glownia, A. J. Taylor, and G. Rodriguez, Opt. Express **15**, 4577 (2007).
[20] P. B. Corkum, Phys. Rev. Lett. **71**, 1994 (1993).
[21] T. Brabec and F. Krausz, Rev. Mod. Phys **72**, 545 (2000).
[22] M. Lewenstein, P. Balcou, M. Y. Ivanov, A. LHuillier, and P. B. Corkum, Phys. Rev. A. **49**, 2117 (1994).
[23] E. L. Falcão Filho, M. Gkortsas, A. Gordon, and F. X. Kärtner, Opt. express **17**, 11217 (2009).
[24] E. L. Falcao-Filho, C. J. Lai, K. H. Hong, V. M. Gkortsas, S. W. Huang, L. J. Chen, and F. X. Kärtner, Appl. Phys. Lett. **97**, 061107 (2010).
[25] J. L. Krause, K. J. Schafer, and K. C. Kulander, Phys. Rev. Lett. **68**, 3535 (1992).
[26] C. Figueira de Morisson Faria, M. Dörr, and W. Sandner, Phys. Rev. A **55**, 3961 (1997).
[27] D. Bauer and P. Koval, Comput. Phys. Commun. **174**, 396 (2006).
[28] N. Dudovich, O. Smirnova, J. Levesque, Y. Mairesse, M. Y. Ivanov, D. M. Villeneuve, and P. B. Corkum, Nat. Phys. **2**, 781 (2006).
[29] G. Doumy, J. Wheeler, C. Roedig, R. Chirla, P. Agostini, and L. F. DiMauro, Phys. Rev. Lett. **102**, 093002 (2009).
[30] Y. Oishi, M. Kaku, A. Suda, F. Kannari, and K. Midorikawa, Opt. Express. **14**, 7230 (2006).
[31] X. He, J. M. Dahlström, R. Rakowski, C. M. Heyl, A. Persson, J. Mauritsson, and A. L'Huillier, Phys. Rev. A **82**, 033410 (2010).
[32] J. Dahlström, A. L'Huillier, and J. Mauritsson, Phys. Rev. A. **44**, 095602 (2011).
[33] M. Kress, T. Löffler, S. Eden, M. Thomson, and H. G. Roskos, Opt. Lett. **29**, 1120 (2004).
[34] X. Xie, J. Dai, and X.-C. Zhang, Phys. Rev. Lett. **96**, 075005 (2006).
[35] K. Y. Kim, A. J. Taylor, J. H. Glownia, and G. Rodriguez, Nat. Photon. **2**, 605 (2008).
[36] W. Wang, Z. Sheng, H. Wu, M. Chen, C. Li, J. Zhang, and K. Mima, Opt. Express **16**, 16999 (2008).
[37] J. Dai, N. Karpowicz, and X. C. Zhang, Phys. Rev. Lett. **103**, 023001 (2009).
[38] P. Salières, A. L'Huillier, and M. Lewenstein, Phys. Rev. Lett. **74**, 3776 (1995).
[39] A. Chudinov, Y. Kapitzky, A. Shulginov, and B. Zel'dovich, Opt. and Quant. Elec. **23**, 1055 (1991).
[40] M. V. Ammosov and V. P. Krainov, Sov. Phys.JETP, 1191 **64**, 4 (2013).
[41] A. Scrinzi, M. Geissler, and T. Brabec, Phys. Rev. Lett. **83**, 706 (1999).
[42] D. Zhang, Z. Lü, C. Meng, X. Du, Z. Zhou, Z. Zhao, and

J. Yuan, Phys. Rev. Lett. **109**, 243002 (2012).